

Restricted rupture evolution of the 2022 *M*_w 6.7 Luding China earthquake

Yaping Hu¹, Yuji Yagi^{*2,3}, Ryo Okuwaki^{2,3}, Ryo Yamaguchi⁴, Hangyu Gao⁵

¹School of Geophysics and Measurement-control Technology, East China University of Technology, NO.418, Guanglan Street, Nanchang, Jiangxi, China

²Faculty of Life and Environmental Sciences, University of Tsukuba, Tennodai 1-1-1, Tsukuba, Ibaraki 305–8572, Japan

³Mountain Science Center, University of Tsukuba, Tennodai 1-1-1, Tsukuba, Ibaraki 305–8572, Japan

⁴College of Geoscience, School of Life and Environmental Sciences, University of Tsukuba, Tennodai 1-1-1, Tsukuba, Ibaraki 305–8572, Japan

⁵Graduate School of Science and Technology, University of Tsukuba, Tennodai 1-1-1, Tsukuba, Ibaraki 305–8572, Japan

* Corresponding author (yagi-y@geol.tsukuba.ac.jp)

Summary

On September 5, 2022, a strike-slip earthquake with a moment magnitude (M_w) 6.7 occurred along the Moxi segment of the Xianshuihe fault zone in Luding, Sichuan province, China. To estimate the rupture evolution of the 2022 Luding earthquake, we inverted teleseismic P -waves by applying the Potency Density Tensor Inversion, a novel method that can estimate fault geometry and source process. We found the rupture process can be divided into two episodes. In the first episode, the initial deep rupture continues for 2 second on a westward tilting fault plane. In the next episode (3 to 7 s), the main rupture propagated along the Xianshuihe fault zone toward the south-southeast and halts ~15 km south-southeast from the epicentre. An isolated rupture also occurred ~10 km west from the Xianshuihe fault zone. The main rupture propagated in a south-southeast direction where strain have been accumulating, and our resolved strike direction rotated counterclockwise as it propagated from the epicentre to south-southeast. The along-strike migration of the main rupture stopped in a region with a complex fault network, and the along-dip migration did not go through the shallow-most region to the surface. Our seismic source model suggests that the 2022 Luding earthquake has failed to cascade up to a larger event, contrary to the last largest 1786 Kangding-Luding earthquake in this region, due to the fault geometry and shallow sedimentary layers inhibiting rupture propagation.

Keywords: Earthquake dynamics, Earthquake source observation, Inverse theory, Waveform inversion, Body waves

Introduction

Seismic source models are not only important for understanding the nature of earthquake, but also provide fundamental data for understanding the tectonics (e.g. [Avouac et al. 2014](#); [Elliott et al. 2016](#); [Hayes, 2017](#)). In recent years, a development of a potency density tensor inversion (PDTI) has made it possible to estimate the source process, including information on fault geometry, by assuming a single model plane (e.g. [Shimizu et al., 2020](#)). The seismic source model obtained by the PDTI should be useful for quickly understanding complex earthquakes because the solution is less disturbed by modelling errors. (e.g. [Okuwaki et al., 2021](#)).

At 12:52 (local time) on September 8th, 2022, the M_s 6.8 Luding earthquake occurred in Luding County, Ganzi Prefecture, Sichuan Province, China ([China Earthquake Administration, 2022a](#)) ([Figure 1a](#)), which caused severe infrastructural damages and casualties ([Zhang et al., 2022](#)). The Global Centroid Moment Tensor (GCMT) solution ([Dziewonski et al. 1981](#), [Ekström et al. 2012](#)) was inferred as a strike-slip rupture; aftershocks determined by [Zhang et al. \(2022\)](#) using the double-difference earthquake location algorithm ([Waldhauser & Ellsworth, 2000](#)) are mainly distributed along the Xianshuihe-Moxi segment trending NWN-SES in the southeast end of the Xianshuihe fault zone ([Wen, 2000](#); [Papadimitriou et al., 2004](#)). There is also a notable aftershock zone around 10 km northwest of the epicentre. In general, shapes of teleseismic body waves are sensitive around nodal shear planes, so a stable analysis of earthquakes on strike-slip faults requires the assumption of a detailed fault plane (e.g., [Shimizu et al., 2020](#)). The PDTI, which does not require such a detailed fault plane setup, is suitable for analysing complex strike-slip earthquakes (e.g. [Yamashita et al., 2021](#); [Tadapnsawut et al., 2022](#)).

The left-lateral Xianshuihe fault zone has a high slip rate of ~ 1 cm/y (e.g. [Shen et al., 2005](#); [Wang et al., 2009](#); [Ji et al., 2020](#)), and is known to have hosted M7 class strike-slip earthquakes with recurrence intervals of 20–30 years (e.g. [Allen et al., 1991](#); [Cheng et al., 2021](#)). It has been suggested that the Coulomb stress changes due to the 2008 Wenchuan earthquake (M_w 8.0) are likely to hasten the earthquake occurrence along the Xianshuihe fault zone (e.g. [Parsons et al., 2008](#); [Toda et al., 2008](#)). The 2022 Luding earthquake is situated around a Moxi segment that was ruptured by the 1786 Kangding-Luding earthquake (M 7.8), the largest earthquake along the Xianshuihe fault zone (e.g. [Cheng et al., 2021](#)). It also had been reported that the rate of slip deficit tends to increase toward the south-

southeast from the epicentre of the Luding earthquake (e.g. [Li & Bürgmann, 2020](#); [Li et al., 2021](#)). Understanding the source process of the 2022 Luding earthquake is hence important for assessing the seismic hazard in this region.

In this study, we inverted teleseismic waveform data from the 2022 Luding earthquake using the PDTI with a time-adaptive smoothing constraint ([Yamashita et al., 2022](#)), and obtained a complex rupture process of the 2022 Luding earthquake. We showed that the major rupture propagated in a south-southeast direction and is halted ~15 km south-southeast from the epicentre. In the major rupture halt zone, the inferred fault plane rotates counterclockwise, corresponds to a complex fault network. Our seismic source model also suggest that the rupture area is confined within deeper than ~3 km. Such the confined nature of the 2022 Luding earthquake can be explained as the rupture being not cascaded up due to the geometric barrier and thick sedimentary layers.

Method and Data

Waveform inversion has been used as a tool to analyse the source processes of large earthquakes (e.g. [Olson & Apsel, 1982](#); [Ji et al., 2002](#); [Dettmer et al., 2014](#)), but it has been pointed out that it is often difficult to analyse stably due to modelling errors (e.g. [Mai et al., 2016](#)). In 2020, a new method to reduce the effects of modelling errors originating from uncertainties in the velocity structure and fault geometry; Potential Density Tensor Inversion (PDTI), has been proposed ([Shimizu et al., 2020](#)). In addition to introducing modelling error due to Green's function uncertainty into the covariance data matrix following [Yagi & Fukahata \(2011\)](#), the PDTI reduces the effect of modelling errors due to uncertainty in the fault geometry by increasing the degrees of freedom of the model. The PDTI represents fault slip as a combination of five basis double couples ([Kikuchi & Kanamori, 1991](#)), and by setting the model degrees of freedom appropriately, it succeeds in extracting fault geometry information that was originally included in the waveform data ([Shimizu et al., 2020](#)). The PDTI can also prevent data overfitting by using the Akaike Bayesian Information Criterion (ABIC), even if the model is set with high degrees of freedom (e.g. [Akaike 1980](#); [Yabuki & Matsu'ura, 1992](#); [Sato et al., 2022](#)). The method has been applied to several earthquakes in the various tectonic environments, and it is proven efficient to illuminate the complex nature of earthquake rupture processes (e.g. [Hu et al., 2021](#); [Okuwaki & Fan, 2022](#); [Yamashita et al., 2022a](#)).

In this study, we apply the PDTI with time-adaptive smoothing (Yamashita et al., 2022b) to the vertical component of tele-seismic P-waves observed at 36 global stations for the 2022 Luding earthquake to estimate its source process. The observed data were converted to velocity waveforms by removing an instrument response, and the data were decimated to a sampling interval of 0.8 s. Although the PDTI does not require a model plane to be strictly aligned to the true fault plane, setting a more realistic plane can reduce modelling errors originating from the difference between the model plane and the true fault plane (Shimizu et al., 2021). In this study, we adopt a 50 km × 20 km vertical main model plane corresponding to the aftershock region along the Xianshuihe fault zone and a 10 km × 20 km vertical additional model plane corresponding to the aftershock region around 10 km northwest of the epicentre (Figure 1b). The strike angles of the main and additional model planes were set to 160° and 70°, respectively, and the space knot interval was set to 2 km. The initial rupture point was set at the relocated hypocentre of the 2022 Luding earthquake determined by Zhang et al. (2022). The maximum rupture-front velocity was set to 4.0 km/s, and the potency-rate-density function at each space knot was represented as a linear B-spline functions with an interval of 0.8 s, assuming a total duration of 15 s. In this study, to make the inverse results easier to interpret, all the basis double couple components were rotated so that one double couple component corresponds to the best-fit double couple of the GCMT solution for the 2022 Luding earthquake. The Green's function was calculated assuming a one-dimensional velocity structure including 3 km sedimentary layer by Xu et al., (2013) (Table S1) using the code of Kikuchi & Kanamori (1991). The attenuation time constant t^* was set to 1 s. In general, the arrival time of the P-wave is perturbed by the effect of 3-D Earth velocity structure. To mitigate this effect, the arrival time of the first P-wave was corrected by manual picking.

Results

Our source model for the 2022 Luding earthquake indicate that rupture occurred on at least two faults. In the main model plane, the rupture mainly propagated south-southeastward from the epicentre. Along the main model, we identified two areas of large slip, locating near the hypocentre with maximum slip of 1.8 m and the southeastern part of the hypocentre with maximum slip of 1.9 m (Figure 2). The focal mechanisms in the major slip area show strike-

slip faulting motion, which are consistent with the assumed main model plane. The areas of major slip near and in the south-southeast of the hypocentre are at depths ranging from 12 to 16 km and shallower than 14 km, respectively (Figure 2). In the additional model plane, the focal mechanisms show the strike-slip faulting motion; the main slip area was located at depth ranging from 10 to 16 km with maximum slip of 1.1 m (Figure 2). Both the main and additional model plane show no large slip propagated to the surface. The estimated total moment tensor calculating by the spatiotemporal integrals of the potency-rate density functions is 1.3×10^{19} Nm (M_w 6.7), which is comparable to the GCMT solution of 1.23×10^{19} Nm (M_w 6.7). In this study, the maximum rupture duration was set at 15 second, but the major rupture ended at around 7 second (Figure 2).

Snapshots of rupture evolution at an interval of 1 s contain two episodes of the rupture in the main model plane (Figure 3). In the first episode (0 to 2 s), the initial rupture propagated deeper than hypocentre, corresponding to the initial peak of the moment-rate function. In the second episode (3 to 7 s), together with the main rupture propagated along the main model plane in south-southeast directions; an isolated rupture occurred in the additional model plane. In the main rupture, the rupture propagates at fast speed in a south-southeasterly direction, but it decelerates rapidly at about 15 km south-southeast of the epicentre, and the rupture does not propagate in a shallow area. On the other hand for the isolated rupture, it is difficult to extract the characteristics of rupture propagation. For all the initial, main, and isolated ruptures, the P-axis is oriented WNW-ESE and the T-axis is oriented NNE -SSW. On the other hand, the B-axis is inclined in the west direction in the initial rupture, but in the main and isolated ruptures, the B-axis is oriented almost vertically (Figure 3). After 7 second, no distinct sub-event is detected, as a small amplitude potency-rate is estimated at two model planes (Figure S1). The observed waveform is explained by a waveform synthesized using the estimated source model (Figure S2).

Discussion

In this study, we applied the PDTI to estimate the source process of the 2022 Luding earthquake, including variations in the focal mechanism. We identify three rupture episodes; initial deep and secondary shallower ruptures on the main model plane and the third isolated rupture occurring on the additional model plane located west of the

epicentre. We further confirm that the location and timing of those rupture episodes are robustly estimated against an alternative structural model of the source region used for calculating Green's function (Figure S3).

For the initial and main ruptures, the nodal plane closest to the model plane can be estimated as the fault plane, since the rupture propagates along the main model plane. The fault plane of the initial rupture is inclined toward the west. On the other hand, the dip of the fault plane of the main rupture is nearly vertical. The strike of the main rupture rotates clockwise from the epicentre to south-southeast (Figure 4). The strike of aftershock distribution also appears to rotate counterclockwise from the epicentre to south-southeast, as well as the strike of the Moxi segment similarly rotates counterclockwise from north to south (Figure 1). Our results and the aftershock distribution suggest that the rupture of the 2022 Luding earthquake suddenly slowed down and stopped in the fault bending region at ~15 km south-southeast of the epicentre. The region where rupture stopped also corresponds to a region where multiple faults join, suggesting that a complex fault structure suppressed dynamic rupture propagation (King & Nábělek, 1985; Duan & Oglesby, 2005; Biasi & Wesnousky, 2016).

The third rupture emerges in an isolated manner during 3–5 s, and we do not see a clear rupture migration along both strike and dip directions. Such the isolated rupture manner of the third episode is additionally testified by adopting an alternative model domain, which is striking parallel to the main model plane (Figures S4 and S5). The result remains the same as we observe for the additional model plane perpendicular to the main model plane. Two possible fault planes can be extracted from the focal mechanism solution for the isolated rupture 10 km northwest of the epicentre, but it is difficult to determine whether the rupture occurred on a fault conjugate or parallel to the Xianshuihe fault zone.

It should be noted that the aftershock can be seen at the north-northwestern end of the main model plane, which does not consistent with our rupture episodes observed near the hypocentre and south-southeast of the epicentre. It is possible that the sub-event could not be detected around the north-northwest aftershock area due to insufficient resolution of the tele-seismic body wave, and/or that the north-northwest aftershock area might be triggered in an area far from the co-seismic slip (e.g. Freed, 2005).

The main rupture of the 2022 Luding earthquake propagated from the hypocentre toward the south-southeast and

shallower side of the main model domain, but no major seismic slip occurred in the area of sedimentary layer shallower than 3 km in depth. From the field investigation, no significant coseismic surface deformation was observed (China Earthquake Administration, 2022b; China Earthquake Administration, 2022c). These results may suggest that dynamic rupture propagation was abruptly decelerated in thick sedimentary layers near the surface.

The 1786 Kangding-Luding earthquake is reported to have simultaneously ruptured the Kangding segment to the north of the 2022 Luding earthquake in addition to the Moxi segment, and the surface ruptures of the 1786 Kangding-Luding earthquake were also reported (e.g. Allen et al., 1991; Wen et al., 2008; Yan & Lin 2017). The 2022 Luding earthquake was prevented from cascading up due to inhibited rupture propagation in the sedimentary layers and in the fault bending region around 15 km south-southeast of the epicentre. In general, in the presence of a geometric barrier caused by variations in strike and dip, the earthquake rupture can be divided into two modes: it can either be promoted to propagate across the barrier or prohibited by the barrier. (e.g. Duan & Oglesby, 2005; Sathiakumar et al., 2020). The former should correspond to the 1786 Kangding-Luding earthquake and the latter to the 2022 Luding earthquake. Since the seismicity is characterized by the pre-existing heterogeneity field along the fault (e.g. Aochi & Ide, 2009), the conditions for cascading up in the Xianshuihe fault zone is important for considering the seismic hazard in this region.

Conclusion

We estimated the rupture evolution including fault geometry of the 2022 Luding earthquake by using the Potency Density Tensor Inversion. The rupture process of the 2022 Luding earthquake involves the main south-southeastern rupture propagation with the two strike-slip rupture episodes along the Xianshuihe fault zone. The initial deep rupture is occurring around hypocentre and the secondary rupture dominates in the shallower and the south-southeastern part, but is not likely breaking the surface. We also found the third strike-slip rupture episode occurring ~10 km northwest from the epicentre, which is isolated from the main Xianshuihe fault zone but is consistent with the aftershock region. The main rupture evolution of the 2022 Luding earthquake is halted ~15 km south from the epicentre, which coincides with the complex fault networks and the dense aftershock activity. Addition to this, the main rupture was sharply

decelerating around sedimentary layer in the shallow-most domain. The rupture evolution of the 2022 Luding earthquake halted from cascading up by the geometric barrier in the complex fault networks and thick sedimentary layers in the shallow-most fault section, which suggests that part of the last largest 1786 Kangding-Luding earthquake section (M 7.8), remains to be ruptured.

The Potency Density Tensor Inversion can stably estimate the source process of complex earthquakes, including information on fault geometry, by setting the model degrees of freedom as appropriate for the analyses of teleseismic body waves. Our source model can also provide some essential information that may contribute to assess the seismic hazards via illuminating causes of rupture stop by e.g., complex fault geometry.

Acknowledgments

We thank Prof. Lihua Fang for sharing the relocated aftershocks. This work has been supported by the Grants-in-Aid for Scientific Research (C) 22K03751. Figures are plotted with matplotlib (Hunter 2007) and Generic Mapping Tools (Wessel et al. 2003). The facilities of IRIS Data Services and specifically the IRIS Data Management Center were used to access the waveforms, related metadata, and derived products used in this study. IRIS Data Services are funded through a Seismological Facilities for the Advancement of Geoscience (SAGE) Award from the National Science Foundation under Cooperative Support Agreement EAR-1851048.

Data availability

Waveform data were downloaded via the IRIS Wilber 3 system (<https://ds.iris.edu/wilber3>) from the following networks: the IRIS/IDA Seismic Network (II; <https://doi.org/10.7914/SN/II>); the Global Seismograph Network (IU; <https://doi.org/10.7914/SN/IU>); the GEOFON Seismic Network (GE; <https://doi.org/10.14470/TR560404>); the Netherlands Seismic and Acoustic Network (NL; <https://doi.org/10.21944/e970fd34-23b9-3411-b366-e4f72877d2c5>); the GEOSCOPE (G; <https://doi.org/10.18715/GEOSCOPE.G>); the Mediterranean Very Broadband Seismographic Network (MN; <https://doi.org/10.13127/SD/fBBBtDtd6q>). The Global Centroid-Moment-Tensor (GCMT) solutions are available at <https://www.globalcmt.org/CMTsearch.html>.

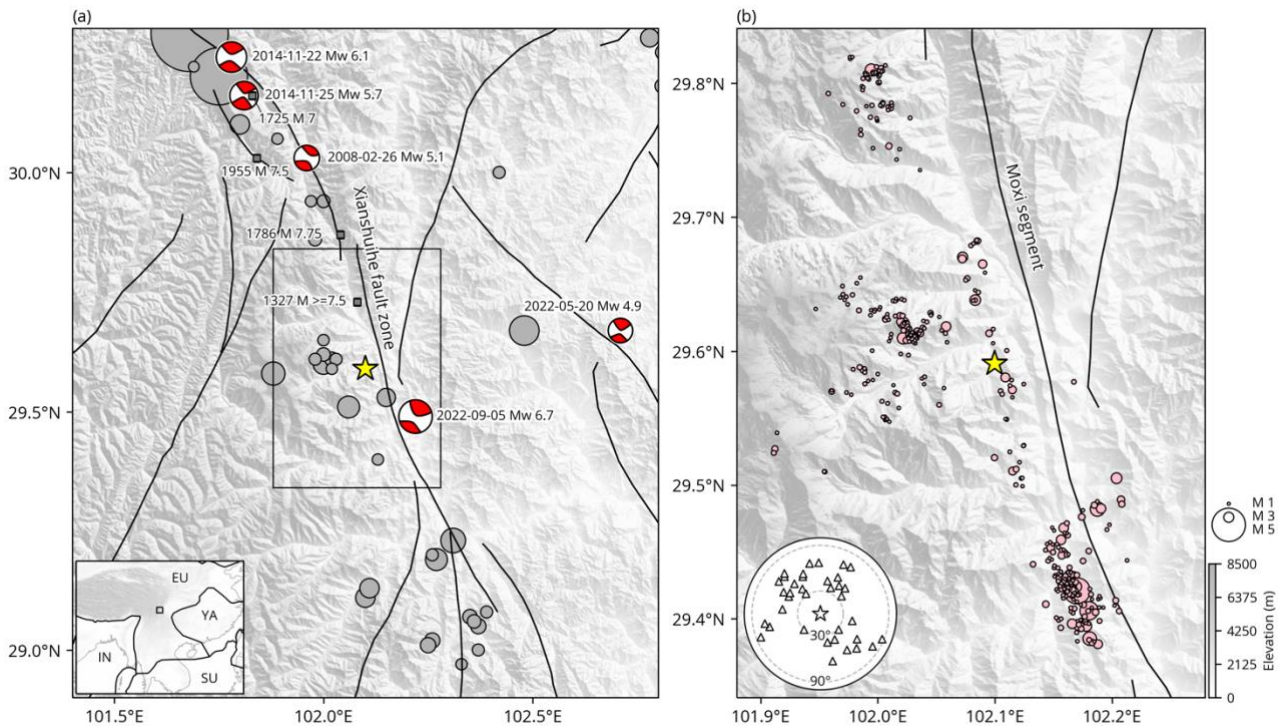


Figure 1. Overview of the study region. (a) The star shows the epicentre of the 2022 Luding earthquake (Zhang et al., 2022). The black lines show the active faults (China Geospatial Data for GMT v0.3.1, 2021). The beachballs are the moment tensor solutions from the GCMT Catalog of depths <70 km between 1976–2022 (Dziewonski et al., 1981; Ekström et al., 2012). The grey circle shows the background seismicity ($M>3.0$; 2009-01-01 to 2022-07-01; China Earthquake Network Center, 2022). The size of the circle scales with its magnitude (see legend). The squares mark the historical earthquakes (Wen et al., 2008). The rectangle outlines the region of Fig. 1b. The topography is from SRTMGL3 data (NASA JPL, 2013b). The inset shows a tectonic setting around the study region. The black lines are the plate boundaries (Bird, 2003). The text denotes the plate name: IN; India, EU; Eurasia, YA; Yangtze, and SU; Sunda plates. The topography is from SRTM15+V2 data (Tozer et al., 2019). The rectangle outlines the region of Fig. 1a. (b) A close-up view of the study region. The circles show 3-day relocated aftershocks (Zhang et al. 2022). The size of the circle scaled with its magnitude (see legend). The topography is from SRTMGL1 data (NASA JPL, 2013a). The inset shows the distribution of the teleseismic stations used in this study. The dashed circles denote the epicentral distances at 30° and 90°. The star denotes the epicentre.

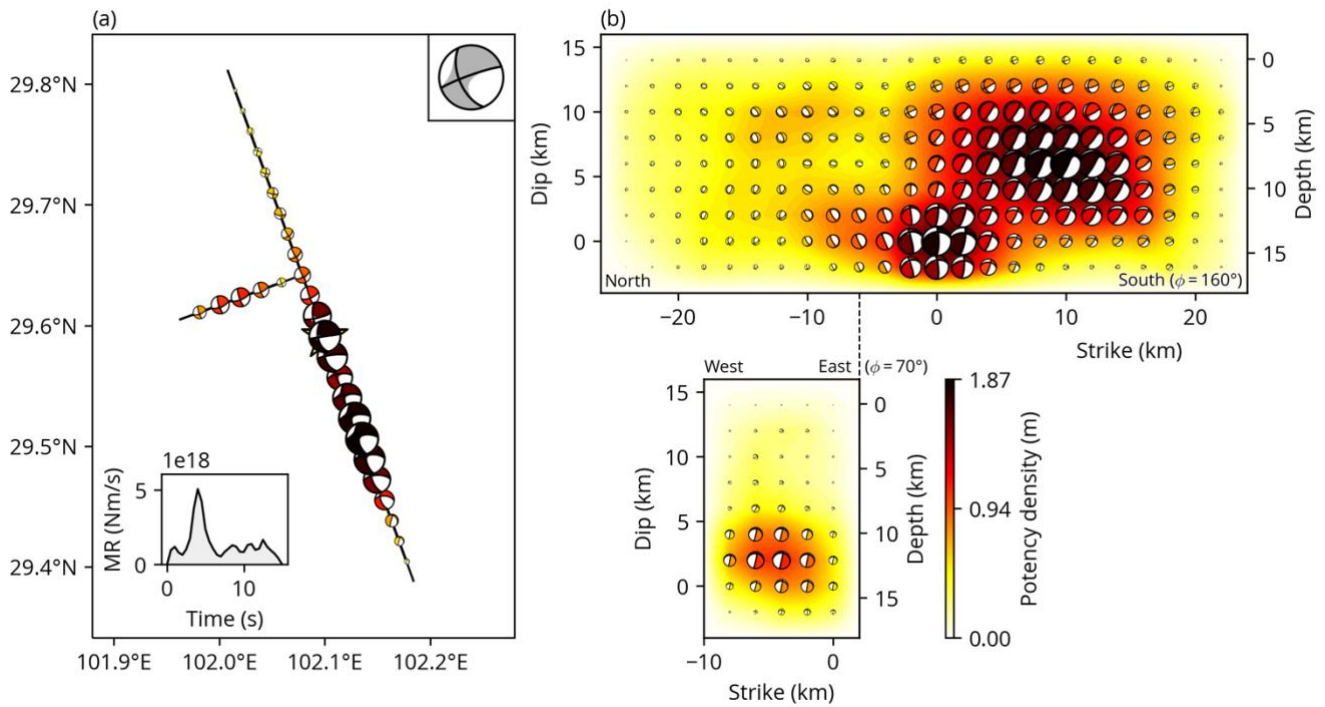


Figure 2. Summary of the inversion result. (a) Potency density tensor distribution in a map view. The star denotes the epicentre. The beach ball in the upper right corner indicates the total moment tensor of our solution. The inset shows the moment-rate (MR) function. The beachballs show the lower-hemisphere projection of the potency density tensor. Only shown are the maximum potency-density tensors along depth (see all the potency density tensors in a cross-sectional view in Fig. 2b). (b) The cross section of the potency density tensor distribution. The strike of the model fault (ϕ) is denoted on each panel. The beachballs in the upper and bottom panels are shown in cross-sectional views from the west-southwest side and south-southeast side, respectively.

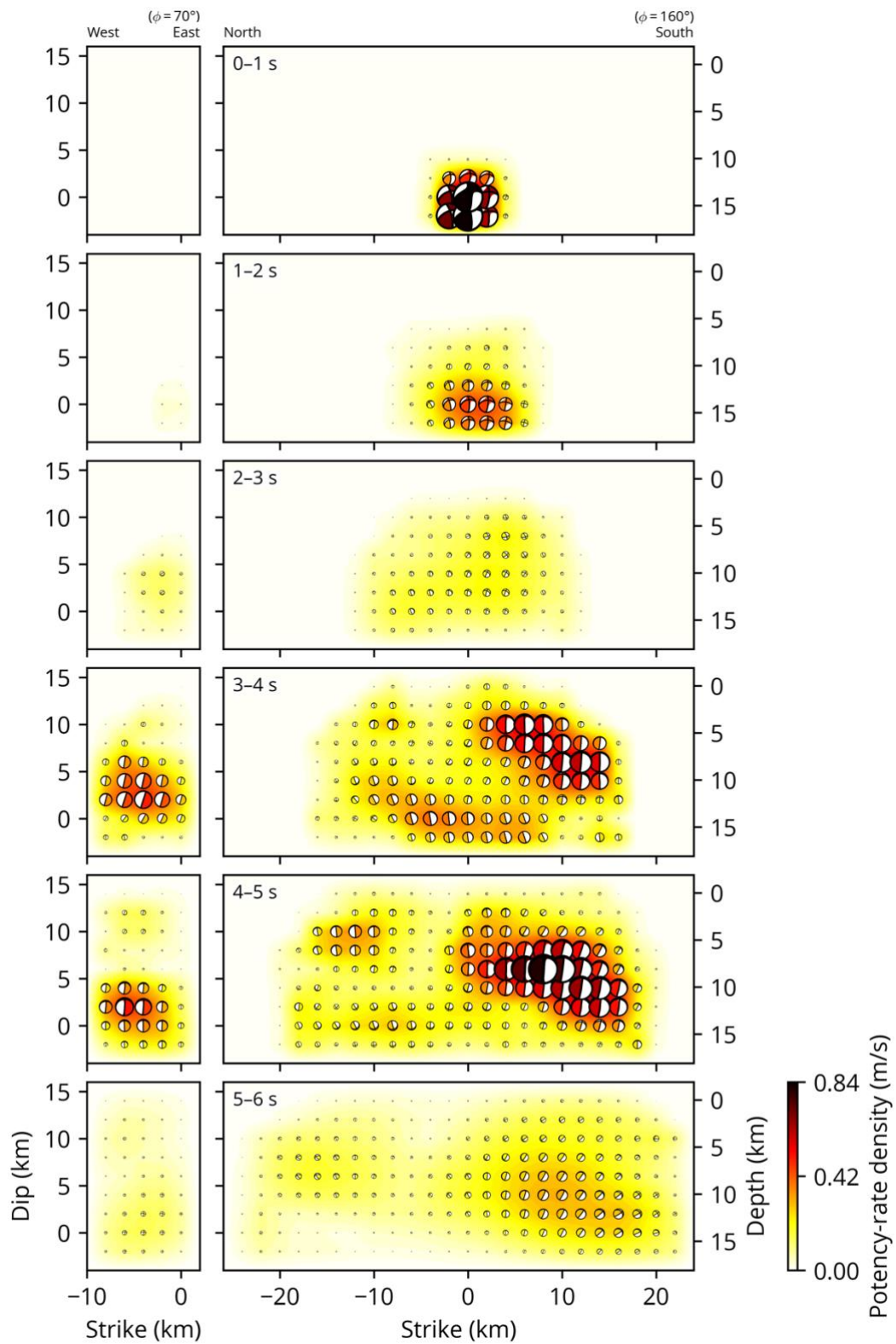


Figure 3. Snapshots of potency-rate density tensor distribution. The strike of the model fault (ϕ) is denoted on each panel. The way of representing potency-rate density tensor (beachball) is the same as for Fig. 2b.

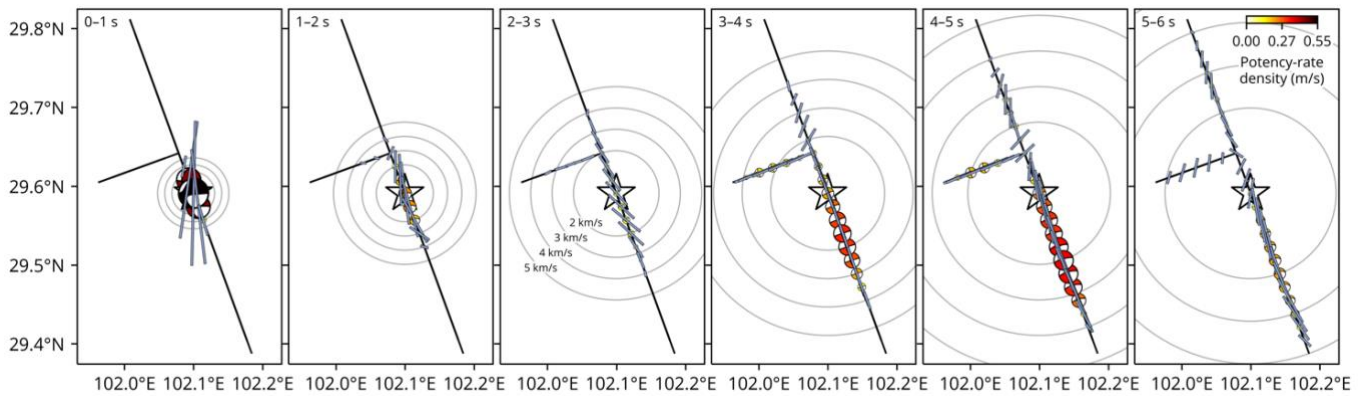


Figure 4. A map view of snapshots of potency-rate density tensor distribution. The star denotes the epicentre. The black lines are the model-fault geometry. The potency-rate density tensor is calculated by averaging the potency-rate density tensors along depth for the corresponding time window shown in upper left of each panel. The blue line represents the orientation of the strike angle, which is estimated from the double-couple solution of the potency-rate density tensor. Only shown is the one for the preferred nodal plane, which maximising the inner product of normal vector with that of the reference model plane. A reference model plane is $\{\text{strike, dip}\} = \{160^\circ, 90^\circ\}$ for the main model fault, and $\{70^\circ, 90^\circ\}$ for the conjugate model fault. The length of the blue line is scaled with its potency-rate density. The grey circles are rupture speeds constantly expanding from the epicentre, which are just for visual references and not related to our source modelling.

References

- Akaike, H. (1980). Likelihood and the Bayes procedure. *Trab. Estad. Y Investig. Oper.*, 31(1), 143–166. <https://doi.org/10.1007/BF02888350>
- Allen, C. R., Zhuoli, L., Hong, Q., Xueze, W., Huawei, Z., & Weishi, H. (1991). Field study of a highly active fault zone: The Xianshuihe fault of southwestern China. *Geological Society of America Bulletin*, 103(9), 1178-1199. [https://doi.org/10.1130/0016-7606\(1991\)103<1178:FSOAHA>2.3.CO;2](https://doi.org/10.1130/0016-7606(1991)103<1178:FSOAHA>2.3.CO;2)
- Aochi, H., & Ide, S. (2009). Complexity in earthquake sequences controlled by multiscale heterogeneity in fault fracture energy. *Journal of Geophysical Research: Solid Earth*, 114(B3). <https://doi.org/10.1029/2008JB006034>
- Avouac, J. P., Ayoub, F., Wei, S., Ampuero, J. P., Meng, L., Leprince, S., ... & Helmberger, D. (2014). The 2013, Mw 7.7 Balochistan earthquake, energetic strike-slip reactivation of a thrust fault. *Earth and Planetary Science Letters*, 391, 128-134. <https://doi.org/10.1016/j.epsl.2014.01.036>
- Biasi, G. P., & Wesnousky, S. G. (2016). Steps and gaps in ground ruptures: Empirical bounds on rupture propagation. *Bulletin of the Seismological Society of America*, 106(3), 1110-1124. <https://doi.org/10.1785/0120150175>
- Bird, P. (2003). An updated digital model of plate boundaries. *Geochem. Geophys. Geosyst.*, 4(3). <https://doi.org/10.1029/2001GC000252>
- Cheng, J., Chartier, T. and Xu, X. (2021). Multisegment Rupture Hazard Modeling along the Xianshuihe Fault Zone, Southeastern Tibetan Plateau. *Seismological Research Letters*, 91(2A), 951-964. <https://doi.org/10.1785/0220200117>
- China Earthquake Administration. (2022a). <https://www.cea.gov.cn/cea/xwzx/369242/5682942/index.html>
- China Earthquake Administration. (2022b). <https://www.eq-igl.ac.cn/kydt/info/2022/37362.html>
- China Earthquake Administration. (2022c). <https://www.eq-igl.ac.cn/kydt/info/2022/37331.html>
- China Earthquake Network Center. (2022). <https://data.earthquake.cn/>
- Chen, G., Xu, X., Wen, X., Chen, Y. (2016). Late Quaternary Slip-rates and Slip Partitioning on the Southeastern Xianshuihe Fault System, Eastern Tibetan Plateau. *Acta Geologica Sinica*, 90(2), 537-553. <https://doi.org/10.1111/1755-6724.12689>
- Dettmer, J., Benavente, R., Cummins, P. R., & Sambridge, M. (2014). Trans-dimensional finite-fault inversion. *Geophysical Journal International*, 199(2), 735-751. <https://doi.org/10.1093/gji/ggu280>
- Dziewonski, A.M., Chou, T.-A. and Woodhouse, J.H. (1981) Determination of earthquake source parameters from waveform data for studies of global and regional seismicity. *Journal of Geophysical Research: Solid Earth*, 86(B4), 2825–2852. <https://doi.org/10.1029/JB086iB04p02825>
- Duan, B., & Oglesby, D. D. (2005). Multicycle dynamics of nonplanar strike-slip faults. *Journal of Geophysical Research: Solid Earth*, 110(B3). <https://doi.org/10.1029/2004JB003298>
- Ekström, G., Nettles, M. and Dziewoński, A.M. (2012). The global CMT project 2004–2010: Centroid-moment tensors for 13,017 earthquakes. *Physics of the Earth and Planetary Interiors*, 200–201, 1–9. <https://doi.org/10.1016/j.pepi.2012.04.002>
- Elliott, J. R., Jolivet, R., González, P. J., Avouac, J. P., Hollingsworth, J., Searle, M. P., & Stevens, V. L. (2016). Himalayan megathrust geometry and relation to topography revealed by the Gorkha earthquake. *Nature*

- Geoscience*, 9(2), 174-180. <https://doi.org/10.1038/ngeo2623>
- Freed, A. M. (2005) Earthquake Triggering by Static, Dynamic, and Postseismic Stress Transfer. *Annual Review of Earth and Planetary Sciences*, 2005, 33:335-367. <https://doi.org/10.1146/annurev.earth.33.092203.122505>
- Hayes, G. P. (2017). The finite, kinematic rupture properties of great-sized earthquakes since 1990. *Earth and Planetary Science Letters*, 468, 94-100. <https://doi.org/10.1016/j.epsl.2017.04.003>
- Hu, Y., Yagi, Y., Okuwaki, R., & Shimizu, K. (2021). Back-propagating rupture evolution within a curved slab during the 2019 Mw 8.0 Peru intraslab earthquake. *Geophysical Journal International*, 227(3), 1602-1611. <https://doi.org/10.1093/gji/ggab303>
- Ji, C., Wald, D. J., & Helmberger, D. V. (2002). Source description of the 1999 Hector Mine, California, earthquake, part I: Wavelet domain inversion theory and resolution analysis. *Bulletin of the Seismological Society of America*, 92(4), 1192-1207. <https://doi.org/10.1785/0120000916>
- Ji, L., Zhang W., Liu C., Zhu L., Xu J., Xu X. (2020) Characterizing interseismic deformation of the Xianshuihe fault, eastern Tibetan Plateau, using Sentinel-1 SAR images. *Advances in Space Research*, 66(2): 378-394. <https://doi.org/10.1016/j.asr.2020.03.043>
- Kikuchi, M., and Kanamori, H. (1991). Inversion of complex body waves. III. *Bulletin of the Seismological Society of America*, 81, 2335–2350. <https://doi.org/10.1785/BSSA0810062335>
- King, G., & Nábělek, J. (1985). Role of fault bends in the initiation and termination of earthquake rupture. *Science*, 228(4702), 984-987. <https://doi.org/10.1126/science.228.4702.984>
- Li, Y., and Bürgmann, R. (2021). Partial coupling and earthquake potential along the Xianshuihe Fault, China. *Journal of Geophysical Research: Solid Earth*, 126(7), e2020JB021406. <https://doi.org/10.1029/2020JB021406>
- Li, Y., Nocquet, J.-M., Shan, X., & Jian, H. (2021). Heterogeneous interseismic coupling along the Xianshuihe-Xiaojiang fault system, eastern Tibet. *Journal of Geophysical Research: Solid Earth*, 126, e2020JB021187. <https://doi.org/10.1029/2020JB021187>
- NASA JPL (2013a). NASA Shuttle Radar Topography Mission Global 1 arc second [Data set]. NASA EOSDIS Land Processes DAAC. Accessed 2022-10-19 from <https://doi.org/10.5067/MEaSURES/SRTM/SRTMGL1.003>
- NASA JPL (2013b). NASA Shuttle Radar Topography Mission Global 3 arc second [Data set]. NASA EOSDIS Land Processes DAAC. Accessed 2022-10-19 from <https://doi.org/10.5067/MEaSURES/SRTM/SRTMGL3.003>
- Mai, P. M., Schorlemmer, D., Page, M., Ampuero, J. P., Asano, K., Causse, M., et al. (2016). The earthquake-source inversion validation (SIV) project. *Seismological Research Letters*, 87(3), 690-708. <https://doi.org/10.1785/0220150231>
- Okuwaki, R., Hirano, S., Yagi, Y., & Shimizu, K. (2020). Inchworm-like source evolution through a geometrically complex fault fueled persistent supershear rupture during the 2018 Palu Indonesia earthquake. *Earth and Planetary Science Letters*, 547, 116449. <https://doi.org/10.1016/j.epsl.2020.116449>
- Okuwaki, R., Hicks, S. P., Craig, T. J., Fan, W., Goes, S., Wright, T. J., & Yagi, Y. (2021). Illuminating a contorted slab with a complex intraslab rupture evolution during the 2021 Mw 7.3 East Cape, New Zealand earthquake. *Geophysical Research Letters*, 48(24), e2021GL095117. <https://doi.org/10.1029/2021GL095117>
- Okuwaki, R., & Fan, W. (2022). Oblique Convergence Causes Both Thrust and Strike-Slip Ruptures During the 2021 M 7.2 Haiti Earthquake. *Geophysical Research Letters*, 49(2), 1–12. <https://doi.org/10.1029/2021GL096373>

- Olson, A. H., & Apsel, R. J. (1982). Finite faults and inverse theory with applications to the 1979 Imperial Valley earthquake. *Bulletin of the Seismological Society of America*, 72(6A), 1969-2001. <https://doi.org/10.1785/BSSA07206A1969>
- Papadimitriou, E., Wen, X., Karakostas, V., Jin, X. (2004). Earthquake triggering along the Xianshuihe fault zone of western Sichuan, China. *Pure and Applied Geophysics*, 161(8): 1683–1707. <https://doi.org/10.1007/s00024-003-2471-4>
- Parsons, T., Ji, C., & Kirby, E. (2008). Stress changes from the 2008 Wenchuan earthquake and increased hazard in the Sichuan basin. *Nature*, 454(7203), 509-510. <https://doi.org/10.1038/nature07177>
- Sato, D., Fukahata, Y., & Nozue, Y. (2022). Appropriate reduction of the posterior distribution in fully Bayesian inversions. *Geophysical Journal International*, 231(2), 1-32. <https://doi.org/10.1093/gji/ggac231>
- Sathiakumar, S., Barbot, S., & Hubbard, J. (2020). Earthquake cycles in fault-bend folds. *Journal of Geophysical Research: Solid Earth*, 125(8), e2019JB018557. <https://doi.org/10.1029/2019JB018557>
- Shen, Z. K., Lü, J. Wang, M. and Bürgmann R. (2005), Contemporary crustal deformation around the southeast borderland of the Tibetan Plateau. *Journal of Geophysical Research*, 110, B11409. <https://doi.org/10.1029/2004JB003421>
- Shimizu, K., Yagi, Y., Okuwaki, R., & Fukahata, Y. (2020). Development of an inversion method to extract information on fault geometry from teleseismic data. *Geophysical Journal International*, 220(2), 1055–1065. <https://doi.org/10.1093/gji/ggz496>
- Shimizu, K., Yagi, Y., Okuwaki, R., & Fukahata, Y. (2021). Construction of fault geometry by finite-fault inversion of teleseismic data. *Geophysical Journal International*, 224(2), 1003-1014. <https://doi.org/10.1093/gji/ggaa501>
- Tadapansawut, T., Yagi, Y., Okuwaki, R., Yamashita, S., & Shimizu, K. (2022). Complex rupture process on the conjugate fault system of the 2014 Mw 6.2 Thailand earthquake. *Progress in Earth and Planetary Science*, 9(1), 1-13. <https://doi.org/10.1186/s40645-022-00484-5>
- Toda, S., Lin, J., Meghraoui, M., Stein, R.S., 2008. 12 May 2008 M = 7.9 Wenchuan, China, earthquake calculated to increase failure stress and seismicity rate on three major fault systems. *Geophysical Research Letters*, 35 (17), L17305. <https://doi.org/10.1029/2008GL034903>
- Tozer, B., Sandwell, D.T., Smith, W.H.F., Olson, C., Beale, J.R., Wessel, P., 2019. Global Bathymetry and Topography at 15 Arc Sec: SRTM15+. *Earth and Space Science* 6, 1847–1864. <https://doi.org/10.1029/2019EA000658>
- Tinti, E., Casarotti, E., Ulrich, T., Taufiqurrahman, T., Li, D., & Gabriel, A. A. (2021). Constraining families of dynamic models using geological, geodetic and strong ground motion data: The Mw 6.5, October 30th, 2016, Norcia earthquake, Italy. *Earth and Planetary Science Letters*, 576, 117237. <https://doi.org/10.1016/j.epsl.2021.117237>
- Waldhauser, F., & Ellsworth, W. L. (2000). A double-difference earthquake location algorithm: Method and application to the northern Hayward fault, California. *Bulletin of the seismological society of America*, 90(6), 1353-1368. <https://doi.org/10.1785/0120000006>
- Wang, H., Wright, T. J., & Biggs, J. (2009). Interseismic slip rate of the northwestern Xianshuihe fault from InSAR data. *Geophysical Research Letters*, 36(3). <https://doi.org/10.1029/2008GL036560>
- Wen, X.Z. (2000). Character of rupture segmentation of the Xianshuihe-Anninghe-Zemuhe fault zone, western

- Sichuan (in Chinese). *Seismology and Geology*, 22(3), 239–249.
- Wen, X. Z., Ma, S. L., Xu, X. W., & He, Y. N. (2008). Historical pattern and behavior of earthquake ruptures along the eastern boundary of the Sichuan-Yunnan faulted-block, southwestern China. *Physics of the Earth and Planetary Interiors*, 168(1-2), 16-36. <https://doi.org/10.1016/j.pepi.2008.04.013>
- Xu, J., Shao, Z. G., Ma, H. S., & Zhang, L. P. (2013). Evolution of Coulomb stress and stress interaction among strong earthquakes along the Xianshuihe fault zone (in Chinese). *Chinese Journal of Geophysics*, 56(4), 1146-1158. <https://doi.org/10.6038/cjg20130410>, retrieved from <http://en.igg-journals.cn/article/doi/10.6038/cjg20130410>
- Yabuki, T., & Matsu'ura, M. (1992). Geodetic data inversion using a Bayesian information criterion for spatial distribution of fault slip. *Geophysical Journal International*, 109(2), 363–375. <https://doi.org/10.1111/j.1365-246X.1992.tb00102.x>
- Yagi, Y., & Fukahata, Y. (2011). Introduction of uncertainty of Green's function into waveform inversion for seismic source processes. *Geophysical Journal International*, 186(2), 711–720. <https://doi.org/10.1111/j.1365-246X.2011.05043.x>
- Yamashita, S., Yagi, Y., Okuwaki, R., Shimizu, K., Agata, R., & Fukahata, Y. (2021). Consecutive ruptures on a complex conjugate fault system during the 2018 Gulf of Alaska earthquake. *Scientific Reports*, 11(1), 1-9. <https://doi.org/10.1038/s41598-021-85522-w>
- Yamashita, S., Yagi, Y., Okuwaki, R., Shimizu, K., Agata, R., & Fukahata, Y. (2022a). Potency density tensor inversion of complex body waveforms with time-adaptive smoothing constraint. *Geophysical Journal International*, 231(1), 91-107. <https://doi.org/10.1093/gji/ggac181>
- Yamashita, S., Yagi, Y., & Okuwaki, R. (2022b). Irregular rupture propagation and geometric fault complexities during the 2010 Mw 7.2 El Mayor-Cucapah earthquake. *Scientific Reports*, 12(1), 1-10. <https://doi.org/10.1038/s41598-022-08671-6>
- Yan, B., & Lin, A. (2017). Holocene activity and paleoseismicity of the Selaha Fault, southeastern segment of the strike-slip Xianshuihe Fault Zone, Tibetan Plateau. *Tectonophysics*, 694, 302–318. <https://doi.org/10.1016/j.tecto.2016.11.014>
- Zhang, L., Zhou, Y., Zhang, X., Zhu, A., Li, B., Wang, S., Liang, S., Jiang, C., Wu, J., Li, Y., Su, J., Yan, L., Fang, L. (2022). 2022 Luding Ms6.8 earthquake: a strong continental event filling the seismic gap (Preprint, in Chinese). *Scientia Sinica Terrae*. Retrieved from https://www.researchgate.net/publication/363924373_2022_Luding_Ms68_earthquake_a_strong_continental_event_filling_the_seismic_gap